



# Novel and highly efficient cathodes for Li-O<sub>2</sub> batteries: 3D self-standing NiFe@NC-functionalized N-doped carbon nanonet derived from Prussian blue analogues/biomass composites

Shengyu Jing<sup>a,g</sup>, Yongliang Zhang<sup>a</sup>, Fu Chen<sup>b</sup>, Huagen Liang<sup>b,c,\*</sup>, Shibin Yin<sup>d</sup>, Panagiotis Tsiakaras<sup>e,f,g,\*\*</sup>

<sup>a</sup> School of Information and Control Engineering, China University of Mining and Technology, Xuzhou, Jiangsu, 221008, China

<sup>b</sup> Low Carbon Energy Institute, School of Materials Science and Engineering, China University of Mining and Technology, Xuzhou, Jiangsu, 221008, China

<sup>c</sup> Key Laboratory of Coal-based CO<sub>2</sub>Capture and Geological Storage, China University of Mining and Technology, Xuzhou, Jiangsu, 221008, China

<sup>d</sup> Guangxi Key Laboratory of Electrochemical Energy Materials, Collaborative Innovation Center of Sustainable Energy Materials, State Key Laboratory of Processing for Non-Ferrous Metal and Featured Materials, Guangxi University, Nanning 530004, China

<sup>e</sup> Laboratory of Electrochemical Devices based on Solid Oxide Proton Electrolytes, Institute of High Temperature Electrochemistry, RAS, Yekaterinburg 620990, Russia

<sup>f</sup> Laboratory of Materials and Devices for Electrochemical Power Industry, Ural Federal University, 19 Mira Str., Yekaterinburg 620002, Russia

<sup>g</sup> Laboratory of Alternative Energy Conversion Systems, Department of Mechanical Engineering, School of Engineering, University of Thessaly, Pedion Areos 38834, Greece



## ARTICLE INFO

### Keywords:

Li-O<sub>2</sub> battery  
Cathode 3D self-standing  
Prussian blue analogues  
Biomass derived carbon

## ABSTRACT

Traditional 3D self-standing electrodes for lithium-oxygen (Li-O<sub>2</sub>) batteries require a high cost and complex preparation process that restrict their development. Herein, discarded biomass (pomelo peel, PP) is used as raw material and in-situ grew NiFe-Prussian blue analogues on its surface. Then a novel 3D binder-free and self-standing NiFe@NC/PPC electrode is obtained through the carbonization process and directly used as a cathode in Li-O<sub>2</sub> batteries.

Compared with PPC (carbonized pomelo peel) and NiFe@NC/CP (NiFe@NC catalysts coated on carbon paper), NiFe@NC/PPC gathered the advantageous characteristics of i) efficient diffusion rates for O<sub>2</sub>/electrolyte and ii) good catalytic activity for oxygen reduction reaction/oxygen evolution reaction (ORR/OER). The as fabricated Li-O<sub>2</sub> batteries, with NiFe@NC/PPC as cathode, are performed a relatively high specific capacity (13.79 mAh cm<sup>-2</sup>), a long cycle life (290 cycles) at a current density of 0.1 mA cm<sup>-2</sup>. Therefore, considering the convenience of synthesis method and the inexpensive raw materials, this is a feasible way to prepare high performance and low cost cathodes for Li-O<sub>2</sub> batteries.

## 1. Introduction

Lithium-oxygen (Li-O<sub>2</sub>) batteries are considered as the most competitive new-generation second-battery because of their super high theoretical energy density [1–4]. The cathode is the location of electrochemical reaction among Li<sup>+</sup>, O<sup>2-</sup> and electrons, as well as the place of discharge product deposition, which is the decisive component of Li-O<sub>2</sub> batteries [5–7]. With the increase of discharge depth, the insoluble and insulating Li<sub>2</sub>O<sub>2</sub> will grow on the catalytic sites and finally cover the electrode surface and block the mass transfer channels [8,9]. Hence, building a novel cathode with efficient electron transfer rate, Li<sup>+</sup>

transfer and oxygen transmission, and high carrying capacity of discharge products is the way to achieve a superior performance Li-O<sub>2</sub> battery.

In recent decades, a lot of cathodes with 3D self-standing structure have been invented and applied to improve Li-O<sub>2</sub> battery performance [10–12]. Ren et al. [13] developed hierarchically N, S co-doped macro-mesoporous carbon/carbon paper and then decorated with PdNi nanoparticles. The macropores of the porous carbon can provide enough space to accommodate discharge products, while the interconnected pores and channels efficiently facilitate oxygen and electrolyte diffusion. The introduction of PdNi nanoparticles greatly enhance the

\* Corresponding author at: Low Carbon Energy Institute, School of Materials Science and Engineering, China University of Mining and Technology, Xuzhou, Jiangsu, 221008, China.

\*\* Corresponding author at: Laboratory of Alternative Energy Conversion Systems, Department of Mechanical Engineering, School of Engineering, University of Thessaly, Pedion Areos 38834, Greece.

E-mail addresses: [lianghg@cumt.edu.cn](mailto:lianghg@cumt.edu.cn) (H. Liang), [tsiak@uth.gr](mailto:tsiak@uth.gr) (P. Tsiakaras).

catalytic activity for ORR/OER. Zhu et al. [14] directly grow carbon nanotubes on the framework of Ni foam by using phenolic resin as carbon source. They suggested that the hierarchical pores among carbon nanotubes, the macroporous structure of Ni foam and the exclusion of polymer binders facilitate the permeation of  $O_2$  and electrolyte and the transmission of  $Li^+$ , resulting a superior battery performance. Zhao et al. [15] constructed 3D porous N-doped graphene aerogels by interconnected nanocages with the aid of polystyrene sphere@polydopamine. The 3D graphene aerogels possess high specific surface area, well-developed interconnected channels and the full exposure of electrochemically active sites, which expand the three-phase reaction interface and ensure ample space for the  $Li_2O_2$  deposition. The electrospinning technology is suitable for the fabrication of 3D self-standing electrodes for  $Li-O_2$  batteries [16–18]. The micropores formed by the intertwined nanofibers can facilitate the permeability of  $O_2$  across the cathode, while the transition metal nanoparticles embedded in the carbon fibers act as catalytic active sites for  $Li_2O_2$  formation. Luo et al. [19] designed a Pt-Gd alloy polycrystalline thin film/Ni foam composite as the binder/carbon-free air electrode. Owing to the high catalytic activity of the Pt-Gd alloy composite and 3D porous structure, the discharge/charge overpotential maintained at a relatively low level after 100 cycles.

The commercialization of  $Li-O_2$  batteries not only needs to consider their actual energy density, but also the convenience of manufacturing process and the cost of cathodes. Compared with the graphene aerogels, carbon paper, Ni foam and carbon fiber network prepared by electrospinning, biomass carbon can derive from a wide range of sources at low cost.

Biomass in nature exhibits rich and varied morphological and structural characteristics, as well as has abundant heteroatoms such as N, S and P [20–25]. The last years it is found that the production of carbon materials from biomass is highly attractive [26]. It is found that for battery applications, carbons derived from biomass could offer a higher capacity than graphite; this is because biomass intrinsically exhibits molecular structures and architectures, which are favorable for charge transport and storage [27]. Since the raw material is naturally available and are required no difficult approaches to be realized for materials engineering, which itself represent a very economical solution [27]. Zeng et al. [28] prepared N-doped carbon with graphene-like nanosheet structure using nori as the raw materials, which used as the catalysts for  $Li-O_2$  batteries. Li et al. [29] prepared N-doped carbon with 3D porous structure originated from prawn shells, which exhibited a superior electrocatalytic activity toward ORR. Taking into account these factors, we first proposed the direct preparation of 3D self-standing cathodes using biomass [30]. Via a simple pyrolysis method and subsequent NH<sub>3</sub> treatment, a novel 3D self-standing N-doped carbon nanonet derived from silkworm cocoon was developed [30]. Recently, Luo et al. [31] developed a self-standing porous carbon electrode derived from wood. After activation by ammonia, the mass transport and discharge product storage can be further enhanced, as well as improving the catalytic activity. Song et al. [32] synthesized a hierarchically porous and ultra-thick “breathable” wood-based cathode for high-performance  $Li-O_2$  batteries. The open and low-tortuosity micro-channels are similar to the breathing channels for oxygen and shorten the diffusion distance, while the enriched mesoporous structure caused by  $CO_2$  activation largely increased the active sites. Although these 3D cathodes based on biomass-derived carbon delivered exciting battery performances, the synthesis process needs to be further simplified and the performance needs to be further improved.

In this work, we prepared a composite of NiFe@NC core-shell nanoparticles highly dispersed on the self-standing N-doped carbon microtubule network (NiFe@NC/PPC), which derived from the NiFe-Prussian blue analogues/pomelo peel (NiFe-PBA/PP). The as prepared NiFe@NC/PPC cathode integrates the advantages of PPC and NiFe@NC: 1) the relatively open pore structure inherited from pomelo peel provide more efficient transmission for  $O_2$ /electrolyte; 2) the abundant

micropores/mesopores and high specific area form by stacking NiFe@NC nanoparticles extend the three-phase reaction interface; 3) inherited the superior ORR/OER catalytic activity of NiFe@NC catalyst. As a result, the as assembled  $Li-O_2$  batteries with NiFe@NC/PPC cathodes can deliver a superior specific capacity of  $13.79\text{ mA h cm}^{-2}$  and 290 cycles at  $0.1\text{ mA cm}^{-2}$ .

## 2. Experimental section

### 2.1. Materials preparation

All the chemicals were of analytical purity without further purification and the pomelos were bought from local supermarkets. After cleaning, the pomelo skins were peeled off and cut into small wafers with the diameter of 16 mm and thickness of ca. 1–2 mm, named as pomelo peel (PP).

NiFe-PBA/PP precursors were synthesized according to the literature [33]. Typically, 0.87 g of  $Ni(NO_3)_2 \cdot 6H_2O$  and 1.325 g of  $Na_3C_6H_5O_7 \cdot 2H_2O$  were dissolved in deionized (DI) water (20 mL) and then several pieces of pomelo peels were added. After continuous magnetic stirring and ultrasonication for 2 h, a solution, containing 0.6585 g of  $K_3[Fe(CN)_6]$  and 20 mL of distilled water, was slowly added at room temperature. After stirring for 15 min, the mixture was aged for 24 h at room temperature. Then the NiFe-PBA/PP precursors was collected and washed for several times with DI water and ethanol. Afterwards, the final products (NiFe@NC/PPC) were prepared by calcinating the PBA/PP precursors at 700–1000 °C, adopting a heating rate of  $3\text{ }^{\circ}\text{C min}^{-1}$  under  $N_2$  atmosphere. The average mass of all NiFe@NC/PPC cathodes was  $\sim 11.5\text{ mg}$  (8–15 mg). On the contrary, the NiFe@NC powder was prepared under the same conditions but without pomelo peels.

The PPC cathodes were pomelo peels pyrolyzed at the same temperature. The average mass of all PPC cathodes was  $\sim 7.5\text{ mg}$  (5–10 mg).

### 2.2. Material characterization

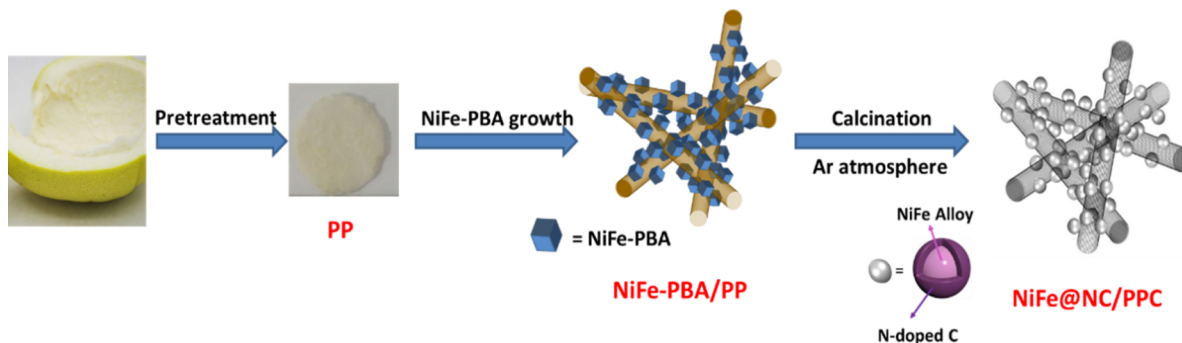
The structure of the cathodes was characterized by X-ray diffraction system (XRD, Bruker D8 Advance) under  $Cu K\alpha$  radiation. The morphology and microstructure of the as-prepared samples were recorded using a Hitachi SU8220 field-emission scanning electron microscope (SEM) and a FEI Tecnai-20 transmission electron microscope (TEM).

X-ray photoelectron spectroscopy (XPS) analysis was carried out by the aid of a ESCALAB 250Xi spectrometer with  $Al K\alpha$  radiation to characterize the chemical compositions. All binding energies were corrected using as a reference the internal standard of the C 1 s peak (284.8 eV). The NiFe load content is obtained by simultaneous thermal analysis (TG/DSC, NETZSCH, TAQ600) from ambient to 800 °C under flowing air.

### 2.3. Electrochemical tests

CR2025-type coin cells with  $7 \times \phi 1.0\text{ mm}$  holes on the positive battery shells were used to perform the electrochemical tests. The self-standing air cathodes (PPC and NiFe@NC/PPC) were served directly as the cathodes. Fresh Li foil was used as the anode, while 1 M  $LiCF_3SO_3$  in tetraethylene glycol dimethyl ether (TEGDME) was used as the electrolyte. Glass filter (Whatman grade GF/D) was employed as the diaphragm to separate the anode and cathode.

In order to demonstrate the superiority of the self-standing electrode, the NiFe@NC powder derived from NiFe-PBA was coated on carbon paper (CP) to prepare NiFe@NC/CP electrode. After the coin cells assembled in an Ar-filled glove box ( $H_2O < 0.5\text{ ppm}$ ,  $O_2 < 0.5\text{ ppm}$ ), all coin cells were sealed in the glass bottle. Then, the glass bottle was transferred out and filled with 1.0 atm of pure  $O_2$ .



**Scheme 1.** The synthesis strategy of 3D self-standing NiFe@NC/PPC cathodes (PP = pomelo peel, PPC carbonized pomelo peel, CP = carbon paper, PBA = Prussian blue analogues).

Before test, the cells were rested for 5 h in  $O_2$  atmosphere.

The discharge/charge behaviors were tested by a battery testing system (Neware, CT-3008, China) between 2.0 and 4.5 V (vs.  $Li^+ / Li$ ) at room temperature. Cyclic stability tests were controlled with a cutoff capacity of  $0.3 \text{ mA h cm}^{-2}$  at a current density of  $0.1 \text{ mA cm}^{-2}$ . Unless otherwise specified, all the specific capacities of the batteries with different cathodes were calculated based on the mass of whole cathode.

The electrochemical impedance spectroscopy (EIS) was performed using a PARSTAT 4000 electrochemical workstation (Princeton, USA), in the frequency range from 100 kHz to 0.1 Hz with a perturbation amplitude of 5 mV. *In-situ* cyclic voltammetry (CV) were conducted at a scan rate of  $0.1 \text{ mV s}^{-1}$  between 2.0 and 4.5 V vs.  $Li^+ / Li$ .

### 3. Results and discussion

**Scheme 1** illustrates the synthesis strategy of 3D self-standing NiFe@NC/PPC cathodes, while Fig. S1 shows the transformation of the samples at different stages of preparation. First, the brown NiFe-PBA cubes deposited on the meridian of white pomelo peels to form NiFe-PBA precursors. After high temperature calcination, the small wafers shrank and became black due to the carbonization of pomelo peel (see Fig. S1).

During carbonization process, Ni ions and Fe ions were reduced by carbon to form NiFe@NC nanoparticles with core-shell structures [34,35]. The finally products maintain their structural integrity all through the preparation and can be directly used as the cathodes of  $Li-O_2$  batteries.

As a proof-of-concept, the electrochemical properties of NiFe@NC/PPC cathodes were analyzed in  $Li-O_2$  batteries at  $0.1 \text{ mA cm}^{-2}$  and the optimal preparation conditions were investigated. Special to note is that the solution A mixed by 0.174 g of  $Ni(NO_3)_2 \cdot 6H_2O$  and 0.265 g of  $Na_3C_6H_5O_7 \cdot 2H_2O$  in 20 ml deionized water and the solution B made from 0.1317 g of  $K_3[Fe(CN)_6]$  in 20 mL of deionized water was recorded as 1-time concentration of NiFe-PBA precursor. In Fig. S2a, it is clear that the optimal calcination temperature of NiFe-PBA/PP is  $1000^\circ\text{C}$ , which may be attributed to the increase of graphitization at higher temperature, resulting in the increase of electrochemical activity. As shown in Fig. S2b, too fast heating rate may cause the collapse of the structure of final electrode and the optimum heating rate is  $5^\circ\text{C min}^{-1}$ . Fig. S2c shows the effect of the concentration of NiFe-PBA precursor solution on the battery performance. With the increase of concentration, the performance of  $Li-O_2$  battery gradually increases. When the concentration of NiFe-PBA precursor solution is 5 times of the initial concentration, the specific capacity of the battery can reach up to  $13.79 \text{ mAh cm}^{-2}$ . Interestingly, it is clear that the platform of discharge gradually increased, while the charge overpotential dramatically varied from 1.23 V to 0.70 V (see Fig. S2d). However, increasing further the concentration of NiFe-PBA precursor solution will worsen the performance of the battery, while the specific capacity is only  $4.94 \text{ mAh cm}^{-2}$ .

with increasing the discharge/charge overpotential. Hence, we conclude that the battery performance is heavily dependent on the loading of NiFe@NC, while the  $O_2$ /electrolyte transmission channel would be blocked by many NiFe@NC nanoparticles, resulting in a poor battery performance. Fig. S3 displays the TG curve of NiFe@NC/PPC cathode, which prepared under the optimal conditions. The content of NiFe alloy in composite materials is only ca. 30%. Unless specified, NiFe@NC/PPC cathodes are prepared under the optimal conditions in the later discussion.

As shown in Fig. 1a, the composition and structure information of the as-prepared NiFe@NC/PPC derives from XRD analysis. The 20 peaks at:  $44.3^\circ$ ,  $51.5^\circ$ , and  $75.8^\circ$  are correlated to the (111), (200), and (220) planes of Awaruite phase  $FeNi_3$  (JCPDS: 38-0419) respectively, while the characteristic peak around  $26^\circ$  can be indexed to the (002) plane of graphitic C.

Then, the morphology of the samples was observed through SEM. As presented in Fig. S4a and S4b, the pomelo peel consists of highly interconnected and well-separated plant fibers prior to calcination process. Moreover, the surface of the fibers is smooth and their average diameter is in the range of  $20\text{--}30 \mu\text{m}$ . After calcination, the plant fibers are converted into carbon microtubules with diameters of about  $20\text{--}30 \mu\text{m}$ , as shown in Fig. S4c.

The carbon microtubules interact with each other to form a 3D network with a large amount of pores and channels, which are conducive enough to enhance the diffusion of oxygen and electrolyte. Similarly, it is clear that the NiFe@NC/PPC electrode maintained the structure of the carbonized pomelo peel (Fig. 1a).

In detail, Figs. 1b and 1c indicates the uniform coverage of NiFe@NC nanoparticles on the surface of microtubules. The average diameter of the nanoparticles is between  $40\text{--}80 \text{ nm}$ . The corresponding EDX elemental mapping (Fig. 1e) demonstrates that C, N, Ni and Fe elements are homogeneously distributed throughout the NiFe@NC/PPC electrode. The low magnification TEM image (Fig. S1) of NiFe@NC/PPC reveals that the NiFe nanoparticles randomly embedded into carbon. As revealed in the high-resolution TEM images of NiFe@NC/PPC (Figs. 2a, & 2b) and the corresponding EDS elemental mapping (Fig. 2c), the NiFe nanoparticle is surrounded by a few graphitic carbon layers. Moreover, the composition of the core can be easily evidenced by the HRTEM image, which shows an interlayer spacing of  $0.203 \text{ nm}$ , corresponding to the (110) planes of the  $FeNi_3$  crystal (Figs. 2a & 2b).

The pore structure of NiFe@NC/PPC cathode and its contrasts (PPC and NiFe@NC/CP) were further confirmed and analyzed by  $N_2$  adsorption technique. From Fig. 3a, it can be seen that PPC exhibited type-IV isotherms and type-H4 hysteresis loop, attributed to slit pores produced by the fragmentation of plant fibers during calcination.

The Brunauer-Emmett-Teller (BET) surface area of PPC is  $160.5 \text{ m}^2 \text{ g}^{-1}$ , and the pore distribution has a broad peak at  $7\text{--}9 \text{ nm}$  calculated from the Barrett-Joyner-Halenda (BJH) method. For the NiFe@NC/CP electrode prepared by coating NiFe@NC powders on

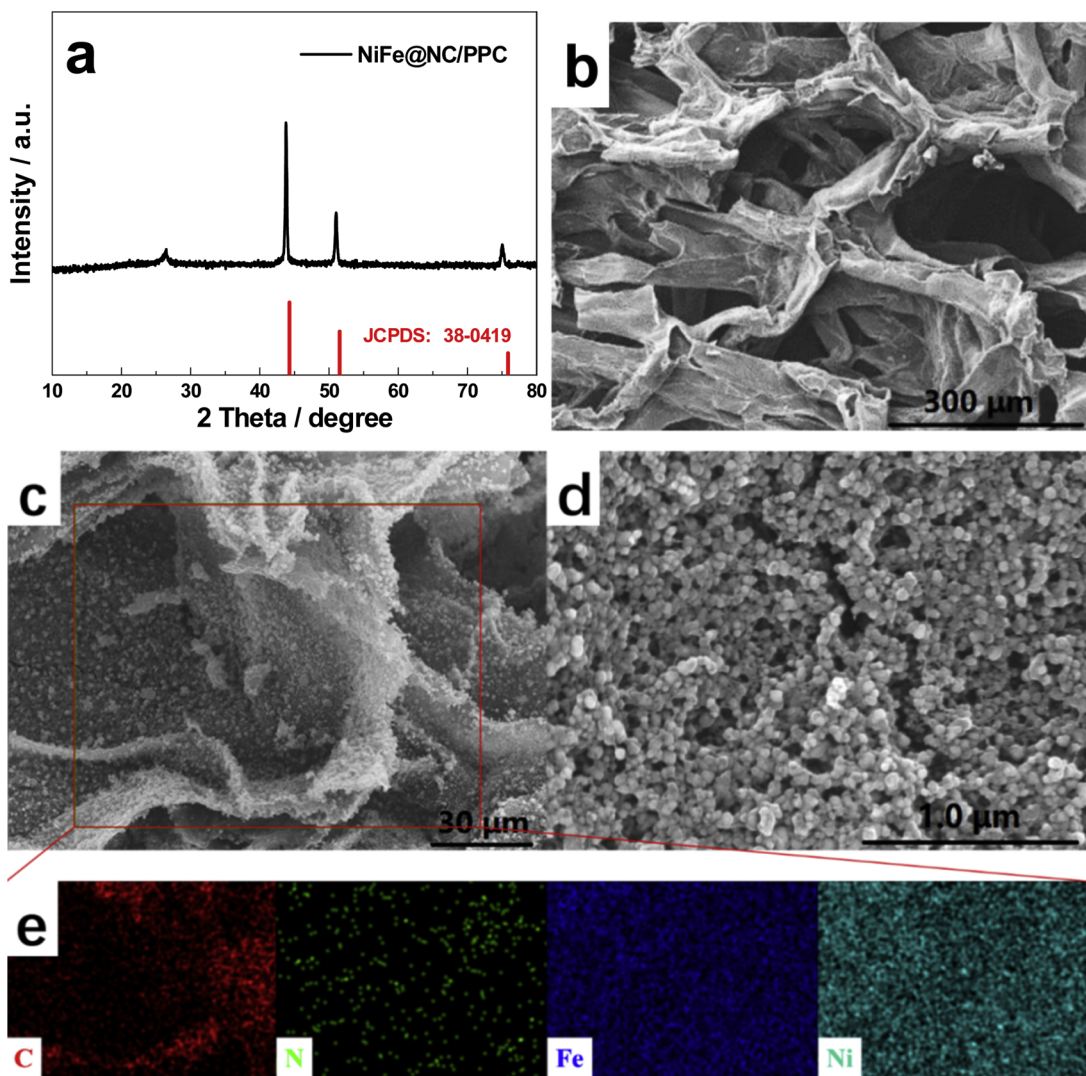


Fig. 1. XRD patterns (a) and SEM images (b, c, d) of NiFe@NC/PPC and element mapping images of NiFe@NC/PPC (e).

carbon paper, the pore size is concentrated between 1–2 nm (Fig. 3b), while the BET surface area is only  $5\text{ m}^2\text{ g}^{-1}$ . Thereby, it can be predicted that NiFe@NC/CP electrode would easily passivated by  $\text{Li}_2\text{O}_2$  during discharging. In contrast, the complex consisting of NiFe@NC and PPC not only inherit the large channel from PPC, but also possess a large amount of micropores and mesopores formed by the accumulation of NiFe@NC nanoparticles.

Because of this, the BET surface area of NiFe@NC/PPC reaches up to  $367.5\text{ m}^2\text{ g}^{-1}$ , which is remarkably higher than that of PPC and NiFe@NC/CP electrode, respectively. In addition, the pore size distribution of NiFe@NC/PPC is within the range of 2–4 nm (Fig. 3b). So, we suggest that the NiFe@NC/PPC cathode integrates the advantages of PPC and NiFe@NC. The relatively open pore structure of NiFe@NC/PPC provides more efficient diffusion for  $\text{O}_2$ /electrolyte compared with NiFe@NC/CP cathode, while the abundant micropores/mesopores and high specific area extend the three-phase reaction interface than PPC cathode, implying an enhanced battery performance.

Raman spectroscopy analyses were conducted to investigate the structural composition of all cathodes, which can influence their catalytic activity. As presented in Fig. 4a, it is clear that two peaks (at  $\sim 1350$  and  $\sim 1580\text{ cm}^{-1}$ ) can be observed for these three electrodes, which can be indexed to the D band and G band, respectively.

Further, the Raman spectra can be fitted with four or five bands (D1, D2, D3, D4, and G) for each sample [36,37]. Among them, the G band corresponds to the defect-free  $\text{sp}^2$  carbon networks with  $\text{E}2\text{g}$  symmetry vibration mode, while the D1 band with  $\text{A}1\text{g}$  symmetry vibration mode is associated with the small crystallite sizes, grains, or edge plane defects of graphite domains. The value of  $\text{D}1/\text{G}$  is an important indicator for explaining the density of edge plane defects for carbon materials [37]. Clearly, the intensity ratio of D1 and G band ( $I_{\text{D}1}/I_{\text{G}}$ ) for NiFe@NC/PPC is larger than that of NiFe@NC (Fig. 4b), implying that NiFe@NC/PPC includes more defects than NiFe@NC.

XPS was performed to study the compositions and the corresponding chemical valence states of the as-prepared samples. The entire XPS spectra are initially corrected by the high-resolution C 1s spectrum. From the survey scan spectrum (see Fig. S3), evident peaks of N for all samples are distinguished, indicating that N atoms were incorporated into the bulk phase of the materials.

As seen in Fig. 5a, two main peaks of Ni 2p spectrum located at around 853 and 870 eV correspond to  $\text{Ni}^{\circ}$ . The binding peaks at around 873.5 and 880.1 eV are assigned to the  $\text{Ni} 2\text{p}^{1/2}$  main peaks, due to the surface oxidation [38–40]. Meanwhile, the high-resolution Fe 2p spectrum (Fig. 5b) shows peaks centered at 707.7 and 720.7 eV, which can be indexed to  $\text{Fe}^{\circ} 2\text{p}^{3/2}$ . Whereas, peaks centered at 725.2 eV

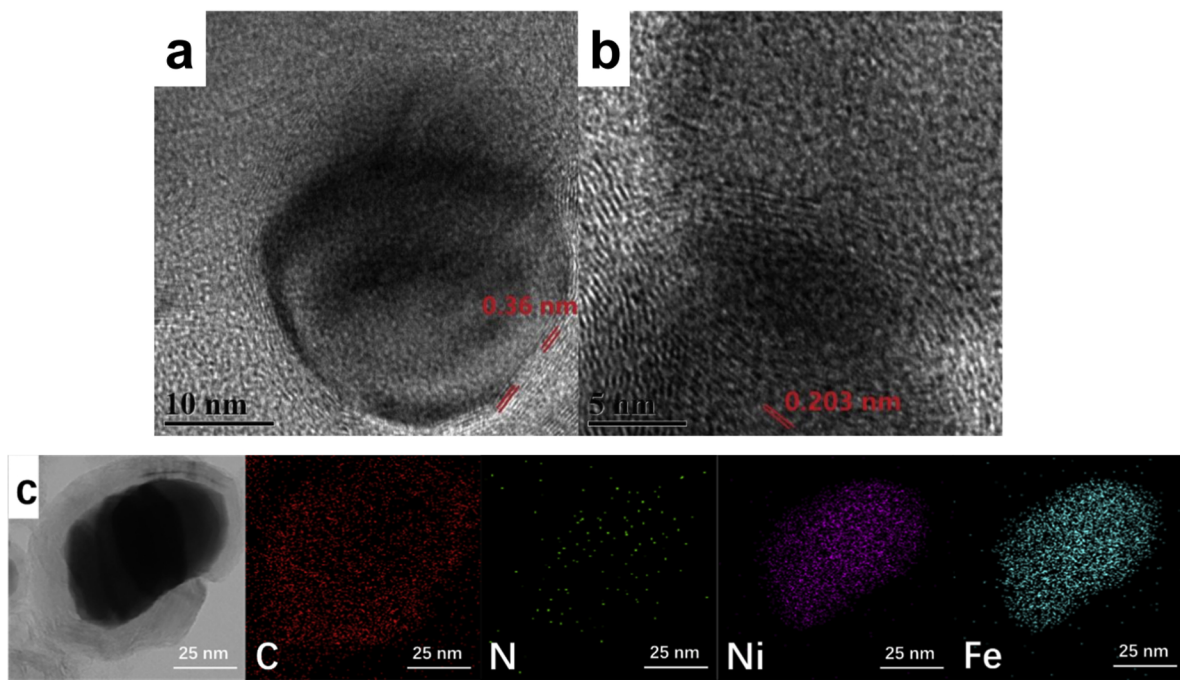


Fig. 2. HR-TEM images of NiFe@NC/PPC (a, b) and EDS mapping of NiFe@NC/PPC (c).

assigned to  $\text{Fe } 2p^{1/2}$  of Fe(III) and Fe(II),  $\approx 711$  to  $\approx 713$  eV assigned to  $\text{Fe } 2p^{3/2}$  of Fe(II) and Fe(III) ions [41,42]. Clearly, we can find that the binding energies of  $\text{Ni}^{\circ}$  and  $\text{Fe}^{\circ}$  of NiFe@NC/PPC shift negatively contrary to NiFe@NC; this is may be due to the strong interaction between NiFe@NC nanoparticles and the pomelo peel carrier during calcination.

The electrocatalytic activity of the different cathodes was examined by cyclic voltammetry (CV), and the results are shown in Fig. 6. It is clear that there is an oxygen reduction current peak for each electrode during the positive scan process, demonstrating that these electrodes possess good catalytic activity for the reaction of oxygen reduction. However, it can be distinguished that the NiFe@NC/PPC catalyst exhibits an ORR onset potential of 2.87 V, which is higher than that of PPC (2.66 V) and of NiFe@NC/CP (2.75 V). Meanwhile, the current density of cathodic peak of NiFe@NC/PPC was significantly higher than

that of the other two electrodes, which proves that the ORR catalytic activity over NiFe@NC/PPC is higher.

Interestingly, although the onset potential of NiFe@NC/CP is higher than that of PPC, its peak current density is lower. We suggested that NiFe@NC has higher catalytic activity than N-doped carbon electrode (PPC). However, enslaved by its electrode structure, the transmission of  $\text{O}_2$ /electrolyte is inefficient, resulting in a larger polarization inside the electrode; so the peak current density is smaller. During the negative scan process, it can be found that NiFe@NC/CP and NiFe@NC/PPC exhibit obvious OER oxidation peaks.

The NiFe@NC/PPC shows a lower OER onset potential of ca. 3.11 V than that of NiFe@NC/CP (ca. 3.35 V), while its anodic peak current density is much higher than that of NiFe@NC/CP. However, the catalytic peak of OER for PPC electrodes is not obvious (see inset of Fig. 6). These results certify that OER/ORR catalytic activity not only depends

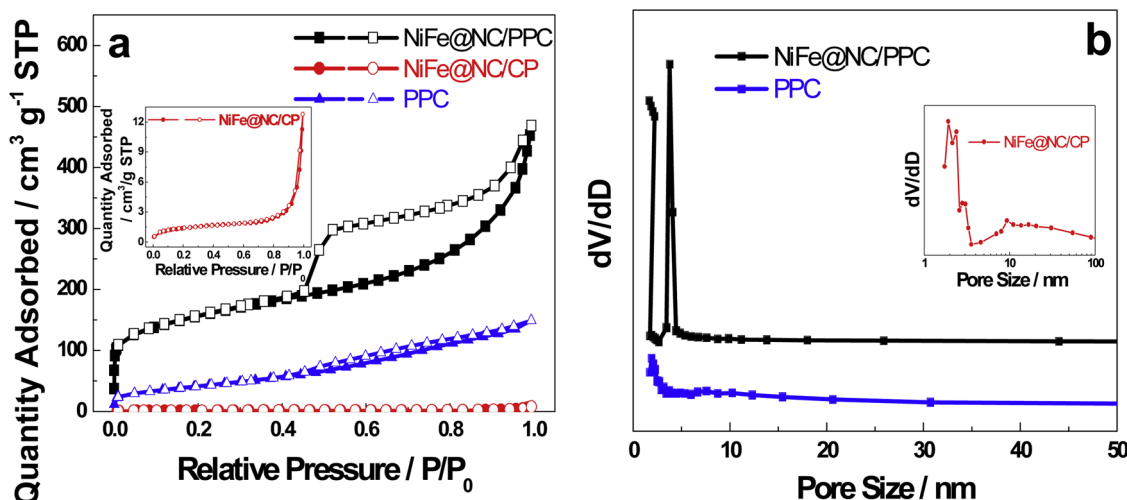


Fig. 3.  $\text{N}_2$  adsorption-desorption isotherms (a) and the pore-size distribution (b) of PPC, NiFe@NC/CP and NiFe@NC/PPC cathodes.

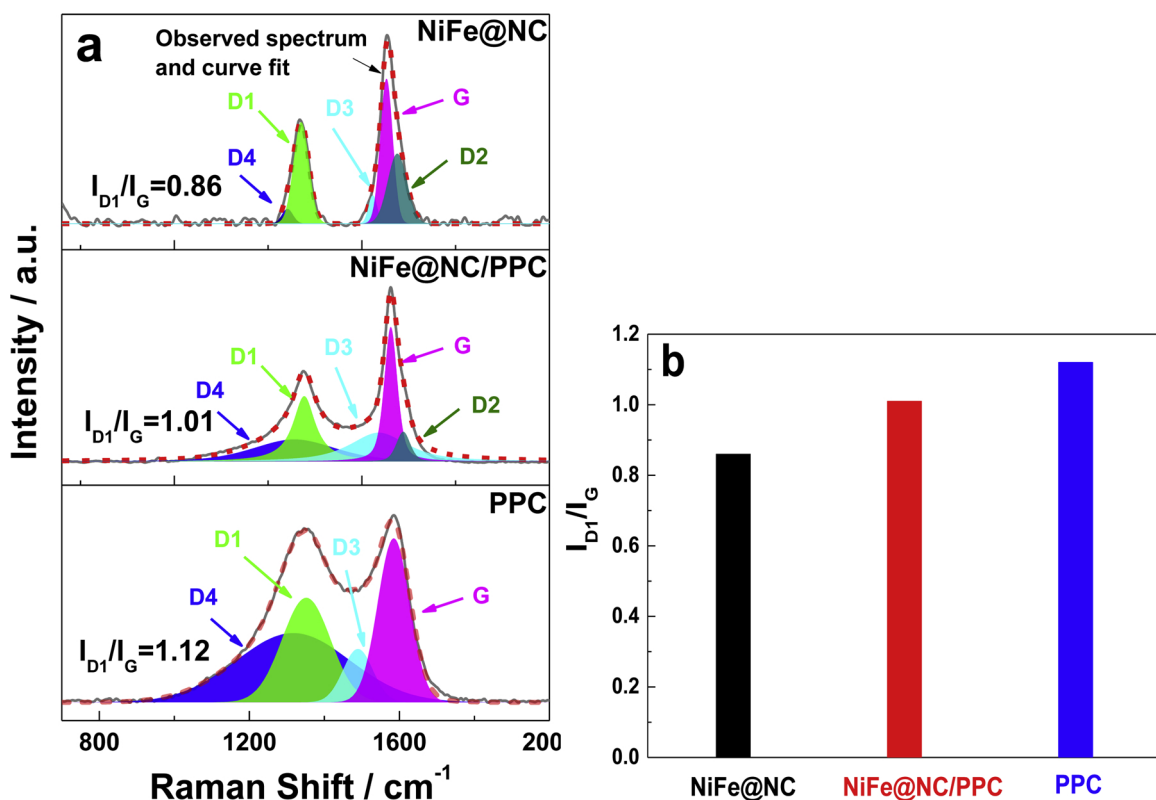


Fig. 4. (a) Curve fitting results for the Raman spectra of PPC, NiFe@NC, and NiFe@NC/PPC samples and (b)  $I_{D1}/I_G$  values of these three cathodes.

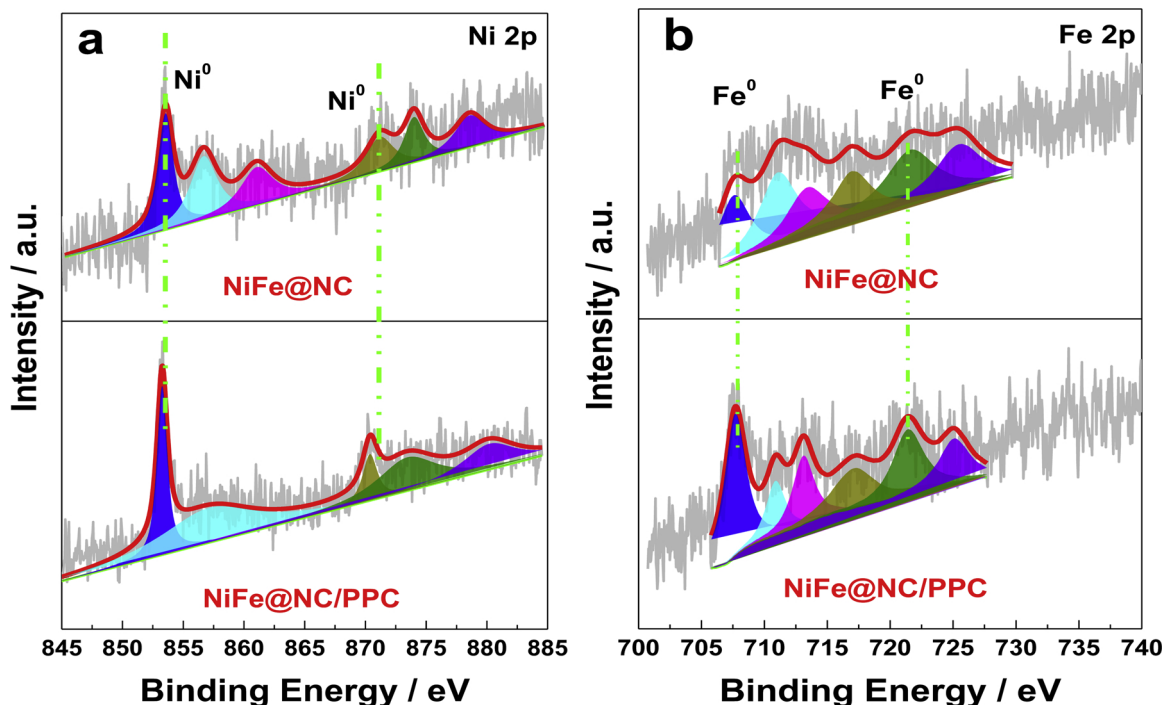


Fig. 5. XPS spectra of NiFe@NC/PPC.

on the physical and chemical properties of the electrode itself, but also on its structure and morphology. NiFe@NC/PPC combines the advantages of NiFe@NC and PPC, which possess excellent catalytic activities and more efficient mass transfer channels.

As a proof-of-concept, the first galvanostatic discharge/charge

curves of NiFe@NC/PPC cathode are then analyzed in  $\text{Li}-\text{O}_2$  batteries. Meanwhile, PPC and NiFe@NC/CP are also employed for comparison. All electrochemical measurements are normalized based on the area of the cathode.

As shown in Fig. 7a, NiFe@NC/PPC cathode delivers a discharge

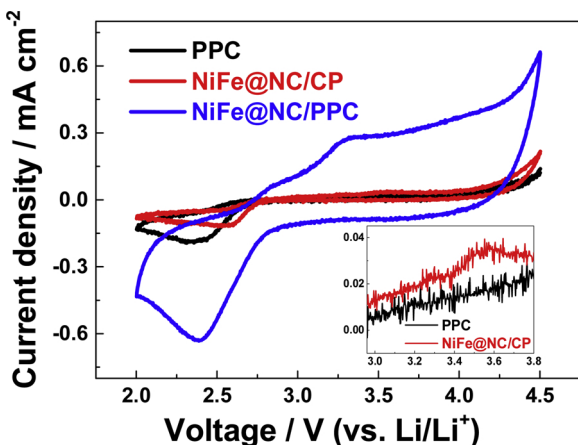


Fig. 6. *In-situ* cyclic voltammetry curves of Li-CO<sub>2</sub> batteries with various cathodes.

specific capacity of 13.79 mA h cm<sup>-2</sup> with a coulombic efficiency of 99.4% at a current density of 0.1 mA cm<sup>-2</sup>.

In addition, the battery with NiFe@NC/PPC cathode shows a stable discharge plateau of ~2.75 V with a corresponding overpotential of ca. 0.21 V. Compared with the data reported in the literature, these results are highly competitive (see Table 1).

In the preceding discussion, we found that NiFe@NC possesses better catalytic activity than PPC, but the small BET specific surface area and the narrow pore size distribution in micropores range are inherent deficiencies for NiFe@NC/CP. Hence, the catalytically active sites and O<sub>2</sub>/electrolyte diffusion channels can be easily covered and blocked by the insoluble insulative discharge products (Li<sub>2</sub>O<sub>2</sub>). However, for PPC cathode, the ORR/OER catalytic activity is poor, which can be proved by the large discharge/charge overpotential.

As such, the cells with NiFe@NC/CP or PPC cathodes show an objective performance. The discharge specific capacity is only 0.83 mA h cm<sup>-2</sup> and 2.49 mA h cm<sup>-2</sup> for PPC and NiFe@NC/CP, respectively, which is almost 1/17 and 1/6 to that of NiFe@NC/PPC. Moreover, the PPC and NiFe@NC/CP cathodes show a much lower coulombic efficiency of 62% and 56%, respectively, revealing the poor reversibility of PPC and NiFe@NC/CP.

The cycling stability of NiFe@NC/PPC cathode was evaluated with a full discharge/charge mode at a current density of 0.1 mA cm<sup>-2</sup>. Evidently, it can be seen from Fig. 7c that the discharge capacity is up to 12.9 mA h cm<sup>-2</sup> after the 2nd cycle and the discharge voltage plateau is stable at around 2.68 V, indicating the good capacity retention ability of NiFe@NC/PPC cathode. Unfortunately, the discharge capacity is faded to 5.7 mA h cm<sup>-2</sup> after 3rd cycle, which is may be due to the fact that the larger Li<sub>2</sub>O<sub>2</sub> particles are not easily decomposed during 1st and 2nd charging process, resulting in the electrode surface passivation. In addition, the decomposition of the electrolyte at high charging voltage may be one of the reasons for the sharp drop in specific capacity. Moreover, the long-term performance of NiFe@NC/PPC cathode was investigated at 0.1 mA cm<sup>-2</sup> with a curtailing capacity of 0.3 mA h cm<sup>-2</sup>, as shown in Fig. 7d. At this capacity, the cathode are far from being deactivated by insulating Li<sub>2</sub>O<sub>2</sub>. Remarkably, the discharge voltage plateau barely drops before 250 cycles, maintaining at ca. 2.7 V. However, the charge potential gradually increases, attributing to the incomplete decomposition of Li<sub>2</sub>O<sub>2</sub>. Notably, the Li-O<sub>2</sub> battery with NiFe@NC/PPC cathode can cycle 290 times and maintain for 1740 h within the voltage window of 2.0 V–4.5 V (Fig. 7e). Under the same conditions, the cycling stability of NiFe@NC/CP it is not worth mentioning (see Fig. S5). The overpotentials of both discharge and charge rapidly increase during cycling, and the battery quickly failed in less than 5 cycles.

In a word, a Li-O<sub>2</sub> battery with NiFe@NC/PPC as cathode exhibits super specific capacity, good rate capability and stable cycling performance, which might be originated from the following aspects: i) the self-standing and binder-free structure of PPC is beneficial to enable rapid oxygen and electrolyte diffusion and to provide enough void space to accommodate Li<sub>2</sub>O<sub>2</sub>; ii) *in-situ* growth of NiFe@NC core-shell catalysts provide strong and stable interconnectivity between the active materials and the support, and more importantly, expand the three-phase reaction interface; and iii) NiFe@NC enhance the ORR/OER catalytic activity compared with N-doped carbon. The synergistic effect between those advantageous factors could realize an efficient formation and decomposition of discharge product Li<sub>2</sub>O<sub>2</sub>.

The reversible formation and decomposition of discharge products were investigated by SEM. Fig. 8a–d show the morphology of discharge product of NiFe@NC/PPC cathode after 1st discharge to 2.0 V at 0.1 mA cm<sup>-2</sup>. It is clear that the insoluble Li<sub>2</sub>O<sub>2</sub> with prefect toroidal structure was deposited on the entire surface of the electrode (Fig. 8a, b). In detail, toroid-shaped Li<sub>2</sub>O<sub>2</sub> and film-like Li<sub>2</sub>O<sub>2</sub> grow tightly on the surface of NiFe@NC catalysts (Fig. 8c, d). Previous reports claim that film-like Li<sub>2</sub>O<sub>2</sub> can be easily decomposed at much lower charge potential than crystalline Li<sub>2</sub>O<sub>2</sub>, due to the enhanced ionic conductivity of film-like Li<sub>2</sub>O<sub>2</sub> [48–51]. In addition, this finding could also explain the charge-discharge curves of Li-O<sub>2</sub> batteries with NiFe@NC/PPC cathode. It is clear that the charge potential is relatively low (< 3.5 V) at the initial stage of charging, as shown in Fig. 7a. We suggest that the film-like Li<sub>2</sub>O<sub>2</sub> coated on the catalyst was first decomposed at the beginning of charging. Then, the crystalline sibling (toroid-shaped Li<sub>2</sub>O<sub>2</sub>) was then decomposed at a higher overpotential. Hence, we can see that the charging potential rises steeply.

After being charged at 4.5 V, almost all of the discharge products disappear, as shown in Fig. 8e & f. Furthermore, it is clear that the NiFe@NC nanoparticles with core-shell structure are re-exposed (Fig. 8g & h), while the porous structure formed by the accumulation of catalyst particles also can be clearly observed. This result indicates the high reversibility of the NiFe@NC/PPC cathode upon cycling. It is believed that the network structured NiFe@NC/PPC cathode provides sufficient space for Li<sub>2</sub>O<sub>2</sub> deposition and enhances the decomposing ability for Li<sub>2</sub>O<sub>2</sub>.

To identify the discharge products during battery operation, XPS analysis was carried out and the results are shown in Fig. 9a. A sharp peak in the Li 1 s XPS spectrum at 54.7 eV can be clearly observed after the 1<sup>st</sup> discharge, indicating that Li<sub>2</sub>O<sub>2</sub> is the main discharge product [52,53].

After recharging, the Li<sub>2</sub>O<sub>2</sub> signal is significantly reduced, suggesting that most of Li<sub>2</sub>O<sub>2</sub> could be decomposed during the recharge process. Instead, the main product is Li<sub>2</sub>CO<sub>3</sub> (55.3 eV), which may be originated from the by-products generated during the charging process, due to the high charge voltage plateau. Electrochemical impedance spectra (EIS) were used to further investigate the rechargeability of the NiFe@NC/PPC cathode. As shown in Fig. 9b and Table S1, the ohmic resistance (R<sub>Ω</sub>) and charge transfer resistance (R<sub>ct</sub>) increased significantly after full discharge, due to the insulating Li<sub>2</sub>O<sub>2</sub> generated on the surface of cathode. After recharging, R<sub>Ω</sub> is a bit larger than the corresponding ones before cycling, due to the Li<sub>2</sub>CO<sub>3</sub> produced by side reactions and residual Li<sub>2</sub>O<sub>2</sub>, which is consistent with the XPS results. Pleasurably, R<sub>ct</sub> almost recovered to the initial value after charging, further demonstrating the superior reversibility of NiFe@NC/PPC.

The chemical states of NiFe@NC/PPC at different stage are also confirmed by XPS measurements. In the Ni 2p spectrum of Fig. 10a, after the 1<sup>st</sup> full discharge, two main peaks located at 854.2 and 861.9 eV are associated with the characteristic peaks of Ni 2p<sup>3/2</sup> and its satellites [54,55], while the Ni 2p<sup>1/2</sup> main peaks and its satellites located at 873.5 and 880.1 eV [56].

The spin-orbit splitting values of Ni 2p<sup>3/2</sup> and 2p<sup>1/2</sup> are over 15 eV, suggesting that these are in the divalent and trivalent states [55]. However, the peaks located at 853.5 eV and 870.3 eV reappeared after

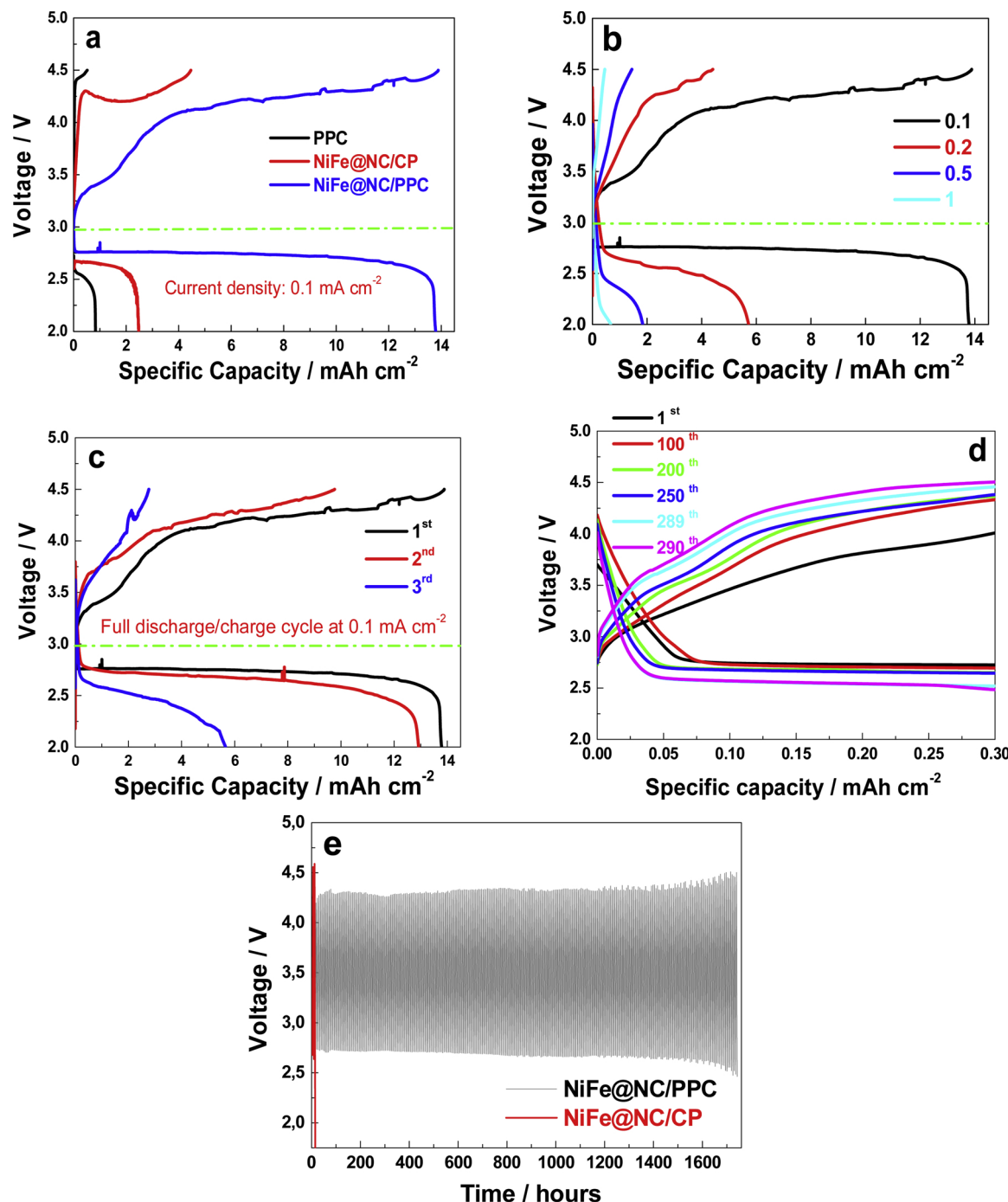


**Fig. 7.** (a) Charge-discharge curves of Li-O<sub>2</sub> batteries with various cathodes; (b) Rate capability of NiFe@NC/PPC cathode at different current densities; (c) The battery performance of NiFe@NC/PPC cathode under full discharge/charge cycling at 0.1 mA cm<sup>-2</sup>; (d) The cycling stability of NiFe@NC/PPC cathode at 0.1 mA cm<sup>-2</sup> with a limited capacity of 0.3 mA h cm<sup>-2</sup>; (e) The variation of the terminal charge and discharge voltages of NiFe@NC/PPC cathode at 0.1 mA cm<sup>-2</sup> with a limited capacity of 0.3 mA h cm<sup>-2</sup>.

recharge, which are corresponding to Ni<sup>+</sup>. Similarly, as shown in Fig. 10b, this situation also can be found on the Fe 2p spectra, indicating that NiFe alloy is the catalytic active center for ORR/OER.

As known, the solution mechanism can well explain the formation of large-sized toroidal-like Li<sub>2</sub>O<sub>2</sub> [57,58]. As shown in Fig. 11, the relatively open pore structure of NiFe@NC/PPC would provide more efficient diffusion channels for O<sub>2</sub>/electrolyte. The dissolved Li<sup>+</sup> and O<sub>2</sub> could combine to convert to LiO<sub>2(sol)</sub> by undergoing a one-electron reduction, followed by the disproportion reaction to form large the

toroidal Li<sub>2</sub>O<sub>2</sub> crystal. In the solution model, the formation of toroidal-like Li<sub>2</sub>O<sub>2</sub> is beneficial to a large specific capacity, but it is also the direct reason for a large charge overpotential, which can be verified in Fig. 7.

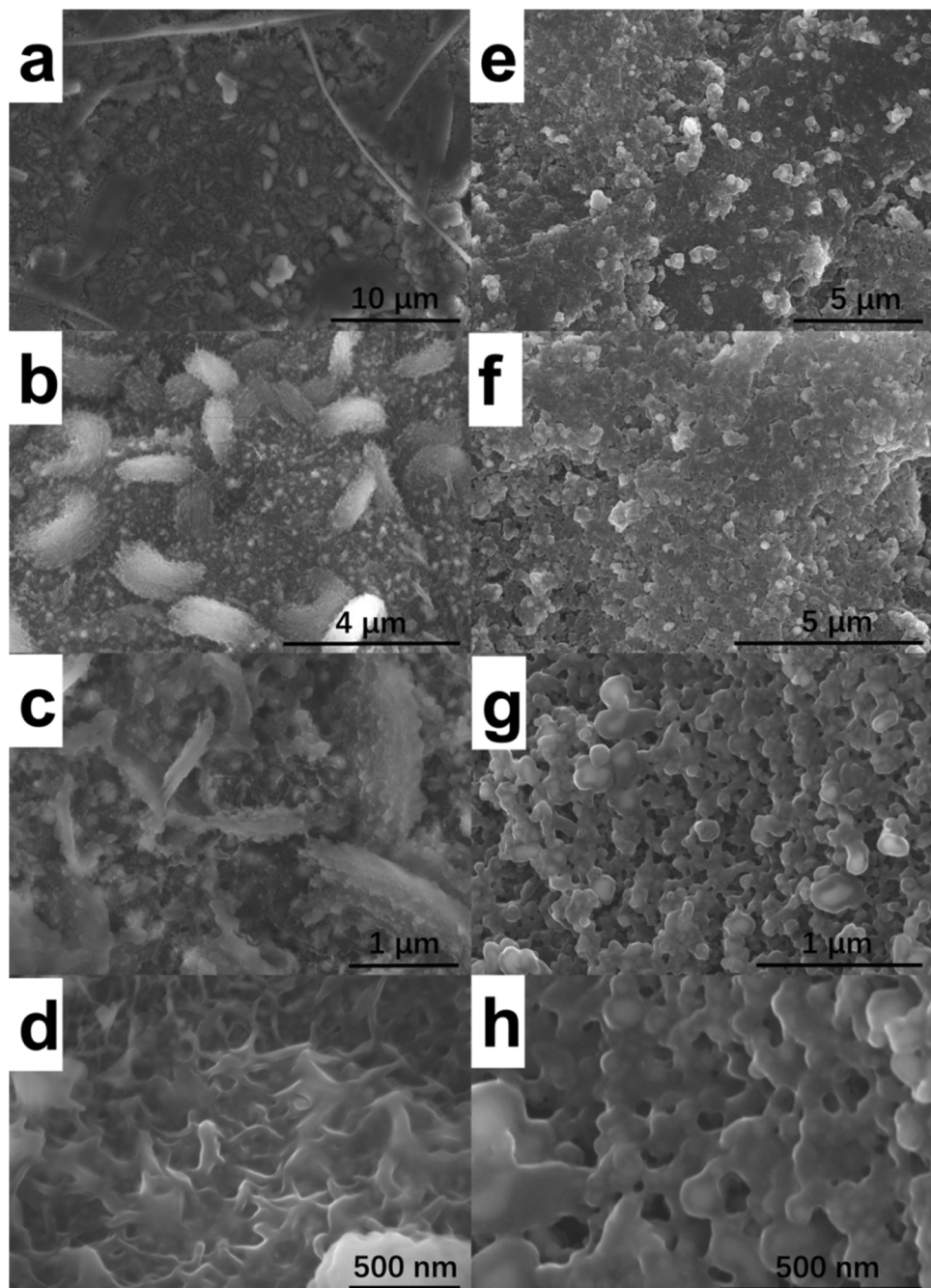
#### 4. Conclusions

In this work, for the first time, we designed a 3D self-standing air electrode for high-performance Li-O<sub>2</sub> batteries, which combines the

**Table 1**The performance of Li-O<sub>2</sub> batteries with different cathodes.

Cathodes	Current density	Specific Capacity (mAh cm <sup>-2</sup> )	Cycle Stability	Refs
Co-N-CNT/CNF	100 mA g <sup>-1</sup> (~0.057 mA cm <sup>-2</sup> )	6.63	130	[43]
Ag/stillage-derived carbon	100 mA g <sup>-1</sup>	Unknown (6000 mA h g <sup>-1</sup> )	94	[44]
Ru/wood-derived carbon	0.1 mA cm <sup>-2</sup>	8.58	100	[32]
Wood-derived N-doped C	0.08 mA cm <sup>-2</sup>	1.86	20	[31]
Biphase N-doped Co@graphene capsule	0.1 mA cm <sup>-2</sup>	5.98	30	[45]
Co-CNFs	0.079 mA cm <sup>-2</sup>	Unknown	70	[18]
Co@N-C microspheres	0.1 mA cm <sup>-2</sup>	3.86	40	[46]
FeCo@N-doped C core-shell composites	0.1 mA cm <sup>-2</sup>	5	40	[47]
NiFe@NC/PPC	0.1 mA cm <sup>-2</sup>	13.79	290	This work

Meanwhile, the NiFe@NC/PPC cathode displays an outstanding rate capability (Fig. 7b). Even at a higher current density of 0.5 mA cm<sup>-2</sup>, the Li-O<sub>2</sub> battery with NiFe@NC/PPC cathode still exhibits an impressive specific capacity of 1.8 mA h cm<sup>-2</sup>.

**Fig. 8.** SEM images of NiFe@NC/PPC cathodes after 1<sup>st</sup> discharge (a–d), and 1<sup>st</sup> charge (e–h).

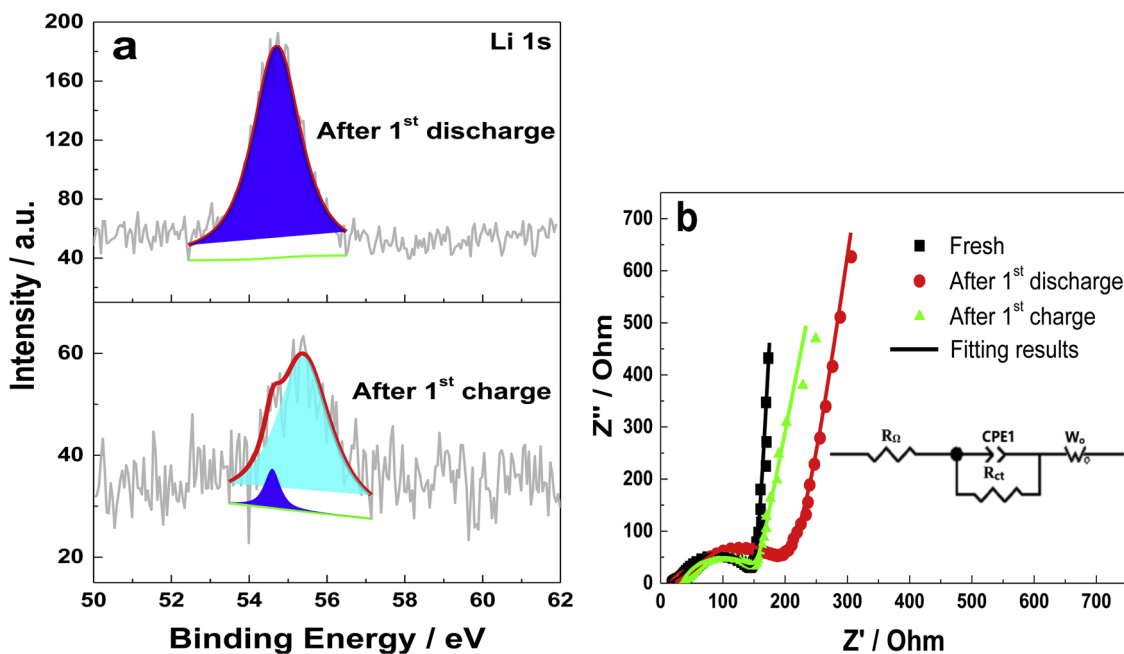


Fig. 9. (a) High-resolution Li 1s spectra of NiFe@NC/PPC after 1<sup>st</sup> full discharge and 1<sup>st</sup> full charge at 0.1 mA cm<sup>-2</sup>. (b) EIS spectra of the NiFe@NC/PPC cathode (the inset shows the corresponding equivalent circuit).

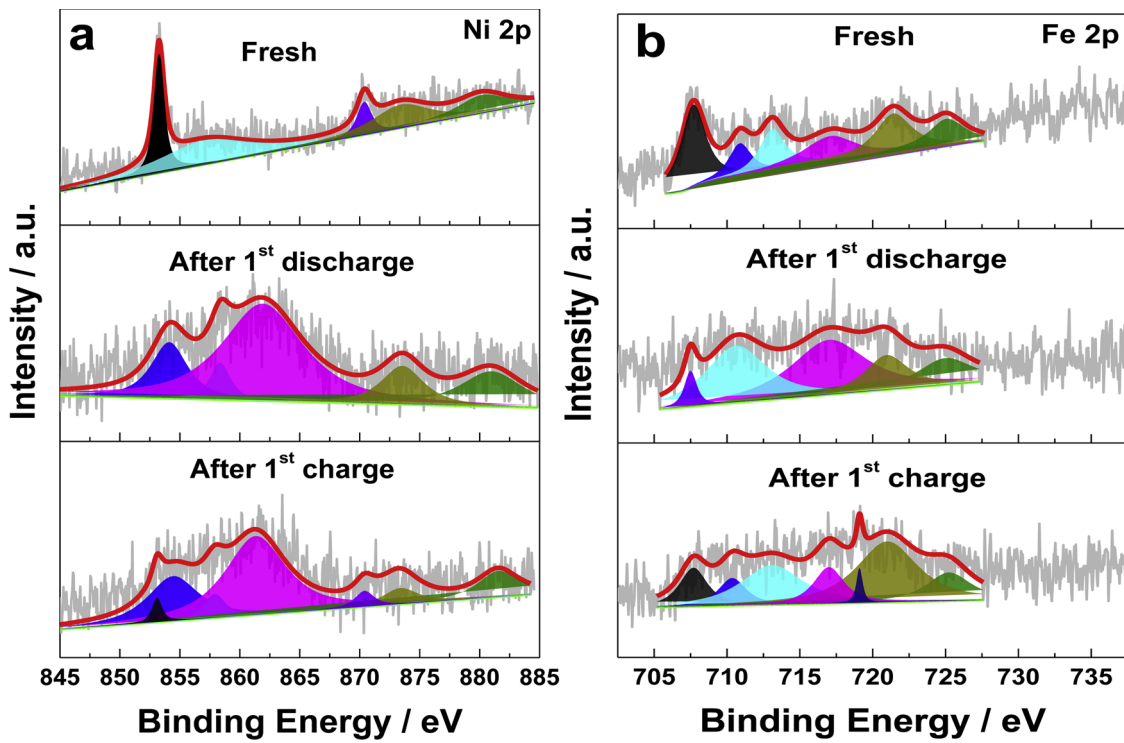


Fig. 10. XPS spectra of Ni 2p (a) and Fe 2p (b) for NiFe@NC/PPC at different stage.

easy synthesis of PBA (Prussian blue analogues) with biomass (pomelo peel). The resultant NiFe@NC/PPC cathode inherited the porous characteristic of biomass, which facilitate the O<sub>2</sub>/electrolyte transmission.

Meanwhile, the NiFe@NC core-shell nanoparticles with an average size of 40–80 nm are well grew on the meridian of pomelo peel-derived carbon nanonet, which can provide a large number of active sites, resulting in an expanded three-phase reactive interface in NiFe@NC/PPC cathode.

Consequently, the Li–O<sub>2</sub> battery with NiFe@NC/PPC cathode shown a high specific capacity, low discharge/charge overpotential and superior cycling performance, attributing to the synergistic effect between NiFe@NC catalyst and PPC support.

Although there is still room for further improvement in battery performance, this low-cost material with a simple and convenient synthesis process may be the ideal one for designing high performance 3D self-standing electrodes of Metal–O<sub>2</sub> batteries, Li-sulfur batteries or other energy storage systems.

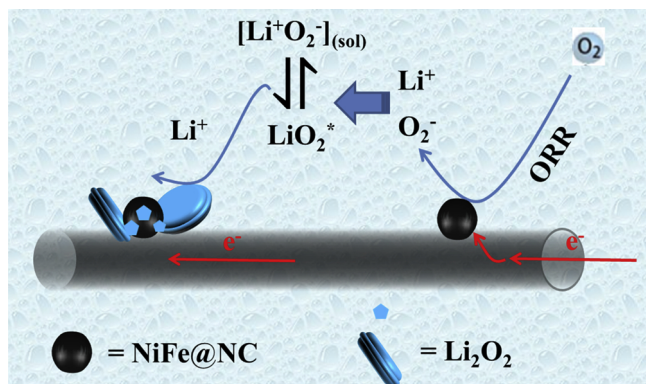


Fig. 11. The mechanism of electrochemical growth of the toroidal-like  $\text{Li}_2\text{O}_2$ .

## Acknowledgments

The authors gratefully acknowledge the Fundamental Research Funds for the Central Universities (2013QNA48), Natural Science Foundation of Jiangsu Province of China (BK20160239), Key Laboratory of Coal-based  $\text{CO}_2$  Capture and Geological Storage, Jiangsu Province (China University of Mining and Technology, 2016B06) and Science and Technology Project of Xuzhou City (KC18063) for financial support of this work. The research of Prof. Tsiaikaras was financially supported by the Ministry of Education and Science of the Russian Federation (Mega-Grant, contract no. 14. Z50.31.0001) and co-financed by the European Union and Greek national funds through the Operational Program Competitiveness, Entrepreneurship and Innovation, under the call RESEARCH-CREATE-INNOVATE (project code: T1EDK-02442).

## Appendix A. Supplementary data

Supplementary material related to this article can be found, in the online version, at doi:<https://doi.org/10.1016/j.apcatb.2019.01.032>.

## References

- Z. Zhao, J. Huang, Z. Peng, Achilles' heel of lithium-air batteries: lithium carbonate, *Angew. Chem.-Int. Ed.* 57 (2018) 3874–3886.
- Y.-B. Yin, X.-Y. Yang, Z.-W. Chang, Y.-H. Zhu, T. Liu, J.-M. Yan, Q. Jiang, A water-/Fireproof flexible lithium-oxygen battery achieved by synergy of novel architecture and multifunctional separator, *Adv. Mater.* 30 (2018) 1703791.
- S. Kumar, A. Jena, Y.-C. Hu, C. Liang, W. Zhou, T.F. Hung, W.S. Chang, H. Chang, R.S. Liu, Cobalt diselenide nanorods grafted on graphitic carbon nitride: a synergistic catalyst for oxygen reactions in rechargeable  $\text{Li}_2\text{O}_2$  batteries, *Chemelectrochem* 5 (2018) 29–35.
- H. Cheng, K. Scott, Selection of oxygen reduction catalysts for rechargeable lithium-air batteries—Metal or oxide? *Appl. Catal. B* 108–109 (2011) 140–151.
- M.-C. Kim, J.-Y. So, S.-H. Moon, S.-B. Han, S. Choi, E.-S. Kim, Y.-K. Shin, J.-E. Lee, D.-H. Kwak, C. Lee, W.-G. Bae, K.-W. Park, Nature inspired cathodes using high-density carbon papers with an eddy current effect for high-rate performance lithium-air batteries, *J. Mater. Chem. A* 6 (2018) 9550–9560.
- M. Kim, E. Yoo, W.-S. Ahn, S.E. Shim, Controlling porosity of porous carbon cathode for lithium oxygen batteries: influence of micro and meso porosity, *J. Power Sources* 389 (2018) 20–27.
- J.-W. Jung, J.-S. Jang, T.G. Yun, K.R. Yoon, I.-D. Kim, Three-dimensional nanofibrous air electrode assembled with carbon nanotubes-bridged hollow  $\text{Fe}_2\text{O}_3$  nanoparticles for high-performance lithium-oxygen batteries, *ACS Appl. Mater. Interfaces* 10 (2018) 6531–6540.
- J. Zhang, P. Li, Z. Wang, J. Qiao, D. Rooney, W. Sun, K. Sun, Three-dimensional graphene- $\text{Co}_3\text{O}_4$  cathodes for rechargeable  $\text{Li}_2\text{O}_2$  batteries, *J. Mater. Chem. A* 3 (2015) 1504–1510.
- C. Yang, R.A. Wong, M. Hong, K. Yamanaka, T. Ohta, H.R. Byon, Unexpected  $\text{Li}_2\text{O}_2$  film growth on carbon nanotube electrodes with  $\text{CeO}_2$  nanoparticles in  $\text{Li}_2\text{O}_2$  batteries, *Nano Lett.* 16 (2016) 2969–2974.
- G. Sun, Q. Zhao, T. Wu, W. Lu, M. Bao, L. Sun, H. Xie, J. Liu, 3D foam-like composites of  $\text{Mo}_2\text{C}$  nanorods coated by N-Doped carbon: a novel self-standing and binder-free  $\text{O}_2$  electrode for  $\text{Li}_2\text{O}_2$  batteries, *ACS Appl. Mater. Interfaces* 10 (2018) 6327–6335.
- Y. He, B. Matthews, J. Wang, L. Song, X. Wang, G. Wu, Innovation and challenges in materials design for flexible rechargeable batteries: from 1D to 3D, *J. Mater. Chem. A* 6 (2018) 735–753.
- P. Zhang, Y. Zhao, X. Zhang, Functional and stability orientation synthesis of materials and structures in aprotic  $\text{Li}-\text{O}_2$  batteries, *Chem. Soc. Rev.* 47 (2018) 2921–3004.
- X. Ren, M. Huang, S. Luo, Y. Li, L. Deng, H. Mi, L. Sun, P. Zhang, PdNi alloy decorated 3D hierarchically N, S co-doped macro-mesoporous carbon composites as efficient free-standing and binder-free catalysts for  $\text{Li}-\text{O}_2$  batteries, *J. Mater. Chem. A* 6 (2018) 10856–10867.
- Q.-C. Zhu, F.-H. Du, S.-M. Xu, Z.-K. Wang, K.-X. Wang, J.-S. Chen, Hydroquinone resin induced carbon nanotubes on Ni foam As binder-free cathode for  $\text{Li}-\text{O}_2$  batteries, *ACS Appl. Mater. Interfaces* 8 (2016) 3868–3873.
- C. Zhao, C. Yu, S. Liu, J. Yang, X. Fan, H. Huang, J. Qiu, 3D porous N-Doped graphene frameworks made of interconnected nanocages for ultrahigh-rate and long-life  $\text{Li}-\text{O}_2$  batteries, *Adv. Funct. Mater.* 25 (2015) 6913–6920.
- H. Nie, C. Xu, W. Zhou, B. Wu, X. Li, T. Liu, H. Zhang, Free-standing thin webs of activated carbon nanofibers by electrospinning for Rechargeable  $\text{Li}-\text{O}_2$  batteries, *ACS Appl. Mater. Interfaces* 8 (2016) 1937–1942.
- H. Bo-Wen, L. Xiao-Zhen, W. Hong, W. Chao-Nan, H. Yu-Shi, M. Zi-Feng, Nanofibrous MnNi/CNF composite catalyst for rechargeable  $\text{Li}/\text{O}_2$  cell, *J. Electrochem. Soc.* 160 (2013) A1112–1117.
- Y.-J. Kim, H. Lee, D.J. Lee, J.-K. Park, H.-T. Kim, Reduction of charge and discharge polarization by cobalt nanoparticles-embedded carbon nanofibers for  $\text{Li}-\text{O}_2$  batteries, *ChemSusChem* 8 (2015) 2496–2502.
- W.-B. Luo, X.-W. Gao, D.-Q. Shi, S.-L. Chou, J.-Z. Wang, H.-K. Liu, Binder-free and carbon-free 3D porous air electrode for  $\text{Li}-\text{O}_2$  batteries with high efficiency, high capacity, and Long Life, *Small* 12 (2016) 3031–3038.
- J. Deng, M. Li, Y. Wang, Biomass-derived carbon: synthesis and applications in energy storage and conversion, *Green Chem.* 18 (2016) 4824–4854.
- M. Borghei, J. Lehtonen, L. Liu, O.J. Rojas, Advanced biomass-derived electrocatalysts for the oxygen reduction reaction, *Adv. Mater.* 30 (2017) 1703691.
- T.N. Jebakumar Immanuel Edison, R. Atchudan, N. Karthik, Y.R. Lee, Green synthesized N-doped graphitic carbon sheets coated carbon cloth as efficient metal free electrocatalyst for hydrogen evolution reaction, *Int. J. Hydrogen Energy* 42 (2017) 14390–14399.
- X. Zhao, J. Zhu, L. Liang, C. Li, C. Liu, J. Liao, W. Xing, Biomass-derived N-doped carbon and its application in electrocatalysis, *Appl. Catal. B* 154–155 (2014) 177–182.
- M. Borghei, N. Lauchroen, E. Kibena-Pöldsepp, L.-S. Johansson, J. Campbell, E. Kauppinen, K. Tammeveski, O.J. Rojas, N. Porous, P-doped carbon from coconut shells with high electrocatalytic activity for oxygen reduction: alternative to Pt-C for alkaline fuel cells, *Appl. Catal. B* 204 (2017) 394–402.
- A. Samikannu, L.J. Konwar, P. Mäki-Arvela, J.-P. Mikkola, Renewable N-doped active carbons as efficient catalysts for direct synthesis of cyclic carbonates from epoxides and  $\text{CO}_2$ , *Appl. Catal. B* 241 (2019) 41–51.
- P. Kalyani, A. Anitha, Biomass carbon & its prospects in electrochemical energy systems, *Int. J. Hydrogen Energy* 38 (2013) 4034–4045.
- Y. Yao, F. Wu, Naturally derived nanostructured materials from biomass for rechargeable lithium/sodium batteries, *Nano Energy* 17 (2015) 91–103.
- X. Zeng, L. Leng, F. Liu, G. Wang, Y. Dong, L. Du, L. Liu, S. Liao, Enhanced  $\text{Li}-\text{O}_2$  battery performance, using graphene-like nori-derived carbon as the cathode and adding  $\text{LiI}$  in the electrolyte as a promoter, *Electrochim. Acta* 200 (2016) 231–238.
- Y. Li, H. Zhang, P. Liu, Y. Wang, H. Yang, Y. Li, H. Zhao, Self-supported bimodal-pore structured nitrogen-doped carbon fiber aerogel as electrocatalyst for oxygen reduction reaction, *Electrochim. commun.* 51 (2015) 6–10.
- S. Jing, M. Zhang, H. Liang, B. Shen, S. Yin, X. Yang, Facile synthesis of 3D binder-free N-doped carbon nanonet derived from silkworm cocoon for  $\text{Li}-\text{O}_2$  battery, *J. Mater. Sci.* 53 (2018) 4395–4405.
- J. Luo, X. Yao, L. Yang, Y. Han, L. Chen, X. Geng, V. Vattipalli, Q. Dong, W. Fan, D. Wang, H. Zhu, Free-standing porous carbon electrodes derived from wood for high-performance  $\text{Li}-\text{O}_2$  battery applications, *Nano Res.* 10 (2017) 4318–4326.
- H. Song, S. Xu, Y. Li, J. Dai, A. Gong, M. Zhu, C. Zhu, C. Chen, Y. Chen, Y. Yao, B. Liu, J. Song, G. Pastel, L. Hu, Hierarchically Porous, Ultrathick, "Breathable" Wood-Derived Cathode for Lithium-Oxygen Batteries, *Adv. Energy Mater.* 8 (2018) 1701203.
- C. Xuan, J. Wang, W. Xia, Z. Peng, Z. Wu, W. Lei, K. Xia, H.L. Xin, D. Wang, Porous structured Ni-Fe-P nanocubes derived from a prussian blue analogue as an electrocatalyst for efficient overall water splitting, *ACS Appl. Mater. Interfaces* 9 (2017) 26134–26142.
- S.G. Peera, J. Balamurugan, N.H. Kim, J.H. Lee, Sustainable synthesis of Co@NC core shell nanostructures from metal organic frameworks via mechanochemical coordination self-assembly: an efficient electrocatalyst for oxygen reduction reaction, *Small* 14 (2018) 1800441.
- H.-H. Zou, C.-Z. Yuan, H.-Y. Zou, T.-Y. Cheang, S.-J. Zhao, U.Y. Qazi, S.-L. Zhong, L. Wang, A.-W. Xu, Bimetallic phosphide hollow nanocubes derived from a prussian-blue-analog used as high-performance catalysts for the oxygen evolution reaction, *Catal. Sci. Technol.* 7 (2017) 1549–1555.
- A. Sadezky, H. Muckenhuber, H. Grothe, R. Niessner, U. Pöschl, Raman micro-spectroscopy of soot and related carbonaceous materials: spectral analysis and structural information, *Carbon* 43 (2005) 1731–1742.
- V. Perazzolo, C. Durante, R. Pilot, A. Paduano, J. Zheng, G.A. Rizzi, A. Martucci, G. Granozzi, A. Gennaro, Nitrogen and sulfur doped mesoporous carbon as metal-free electrocatalysts for the in situ production of hydrogen peroxide, *Carbon* 95 (2015) 949–963.
- J. Zhu, M. Xiao, Y. Zhang, Z. Jin, Z. Peng, C. Liu, S. Chen, J. Ge, W. Xing, Metal-organic framework-induced synthesis of ultrasmall encased NiFe nanoparticles coupling with graphene as an efficient oxygen electrode for a rechargeable Zn-Air

battery, *ACS Catal.* 6 (2016) 6335–6342.

[39] Y. Feng, X.-Y. Yu, U. Paik, N-doped graphene layers encapsulated NiFe alloy nanoparticles derived from MOFs with superior electrochemical performance for oxygen evolution reaction, *Sci. Rep.* 6 (2016) 34004.

[40] J. Wang, S. Mao, Z. Liu, Z. Wei, H. Wang, Y. Chen, Y. Wang, Dominating role of Ni<sup>2+</sup> on the interface of Ni/NiO for enhanced hydrogen evolution reaction, *ACS Appl. Mater. Interfaces* 9 (2017) 7139–7147.

[41] S.H. Ahn, X. Yu, A. Manthiram, "Wiring" Fe-N-x-Embedded Porous Carbon Framework onto 1D Nanotubes for Efficient Oxygen Reduction Reaction in Alkaline and Acidic Media, *Adv. Mater.* 29 (2017) 1606534.

[42] M. Li, T. Liu, X. Bo, M. Zhou, L. Guo, A novel flower-like architecture of FeCo@NC-functionalized ultra-thin carbon nanosheets as a highly efficient 3D bifunctional electrocatalyst for full water splitting, *J. Mater. Chem. A* 5 (2017) 5413–5425.

[43] Z.-D. Yang, X.-Y. Yang, T. Liu, Z.-W. Chang, Y.-B. Yin, X.-B. Zhang, J.-M. Yan, Q. Jiang, In situ CVD derived Co–N–C composite as highly efficient cathode for flexible Li–O<sub>2</sub> batteries, *Small* 14 (2018) 1800590.

[44] Y. Yao, F. Wu, Turning waste chemicals into Wealth-A new approach to synthesize efficient cathode material for an Li–O<sub>2</sub> battery, *ACS Appl. Mater. Interfaces* 9 (2017) 31907–31912.

[45] G. Tan, L. Chong, R. Amine, J. Lu, C. Liu, Y. Yuan, J. Wen, K. He, X. Bi, Y. Guo, H.-H. Wang, R. Shahbazian-Yassar, S. Al Hallaj, D.J. Miller, D. Liu, K. Amine, Toward highly efficient electrocatalyst for Li–O<sub>2</sub> batteries using biphasic N-Doping Cobalt@Graphene multiple-capsule heterostructures, *Nano Lett.* 17 (2017) 2959–2966.

[46] J. Song, X. Lv, Y. Jiao, P. Wang, M. Xu, T. Li, X. Chen, J. Li, Z. Zhang, Catalyst nanoarchitecturing via functionally implanted cobalt nanoparticles in nitrogen doped carbon host for aprotic lithium–oxygen batteries, *J. Power Sources* 394 (2018) 122–130.

[47] H. Wang, F. Yin, P. Lv, T. Fan, X. He, B. Chen, Metal–organic-framework-derived FeCo alloy core@nitrogen-doped carbon shell nanoparticles anchored on carbon nanotubes for rechargeable Li–O<sub>2</sub> battery, *Int. J. Hydrogen Energy* 42 (2017) 2127–2133.

[48] D. Kundu, R. Black, E.J. Berg, L.F. Nazar, A highly active nanostructured metallic oxide cathode for aprotic Li–O<sub>2</sub> batteries, *Energy Environ. Sci.* 8 (2015) 1292–1298.

[49] F. Tian, M.D. Radin, D.J. Siegel, Enhanced charge transport in amorphous Li<sub>2</sub>O<sub>2</sub>, *Chem. Mater.* 26 (2014) 2952–2959.

[50] K.C. Lau, R.S. Assary, P. Redfern, J. Greeley, L.A. Curtiss, Electronic structure of Lithium peroxide clusters and relevance to lithium-air batteries, *J. Phys. Chem. C* 116 (2012) 23890–23896.

[51] Y.L. Zhang, Q.H. Cui, X.M. Zhang, W.C. McKee, Y. Xu, S.G. Ling, H. Li, G.M. Zhong, Y. Yang, Z.Q. Peng, Amorphous Li<sub>2</sub>O<sub>2</sub>: chemical synthesis and electrochemical properties, *Angewandte Chemie-International Edition* 55 (2016) 10717–10721.

[52] H.-S. Shin, G.W. Seo, K. Kwon, K.-N. Jung, S.I. Lee, E. Choi, H. Kim, J.-H. Hwang, J.-W. Lee, A combined approach for high-performance Li–O<sub>2</sub> batteries: a binder-free carbon electrode and atomic layer deposition of RuO<sub>2</sub> as an inhibitor-promoter, *APL Mater.* 6 (2018) 047702.

[53] N. Togasaki, R. Shibamura, T. Naruse, T. Momma, T. Osaka, Prevention of redox shuttle using electropolymerized polypyrrole film in a lithium–oxygen battery, *Appl. Mater.* 6 (2018) 047704.

[54] X. Zhang, C. Wang, H. Li, X.-G. Wang, Y.-N. Chen, Z. Xie, Z. Zhou, High performance Li–CO<sub>2</sub> batteries with NiO-CNT cathodes, *J. Mater. Chem. A* 6 (2018) 2792–2796.

[55] H.-q. Wang, X.-p. Fan, X.-h. Zhang, Y.-g. Huang, Q. Wu, Q.-c. Pan, Q.-y. Li, In situ growth of NiO nanoparticles on carbon paper as a cathode for rechargeable Li–O<sub>2</sub> batteries, *RSC Adv.* 7 (2017) 23328–23333.

[56] X. Wu, S. Li, B. Wang, J. Liu, M. Yu, Graphene foam supported multilevel network-like NiCo<sub>2</sub>S<sub>4</sub> nanoarchitectures for robust lithium storage and efficient ORR catalysis, *New J. Chem.* 41 (2017) 115–125.

[57] N. Mahne, O. Fontaine, M.O. Thotiyil, M. Wilkening, S.A. Freunberger, Mechanism and performance of lithium–oxygen batteries - a perspective, *Chem. Sci.* 8 (2017) 6716–6729.

[58] Z. Lyu, Y. Zhou, W. Dai, X. Cui, M. Lai, L. Wang, F. Huo, W. Huang, Z. Hu, W. Chen, Recent advances in understanding of the mechanism and control of Li<sub>2</sub>O<sub>2</sub> formation in aprotic Li–O<sub>2</sub> batteries, *Chem. Soc. Rev.* 46 (2017) 6046–6072.